Research Collection School Of Computing and Information Systems

School of Computing and Information Systems

6-1996

Study of the B0sB0s oscillation frequency using D-s ℓ+ combinations in Z decays

BUSKULIC, D.; et al.

M. THULASIDAS
Singapore Management University, manojt@smu.edu.sg

Citation
1

Study of the $B^0_s\bar{B}^0_s$ oscillation frequency using $D^-_s l^+$ combinations in Z decays

D. Buskulic, I. de Bonis, D. Decamp, P. Ghez, C. Goy, J.P. Lees, A. Lucotte,
M.N. Minard, P. Odier, B. Pietrzyk, et al.

Study of the $B_s^0 \bar{B}_s^0$ oscillation frequency using $D_s^- \ell^+$ combinations in Z decays

The ALEPH Collaboration

Abstract

A lower limit on the oscillation frequency of the $B_s^0 \bar{B}_s^0$ system is obtained from approximately four million hadronic Z decays accumulated using the ALEPH detector at LEP from 1991 to 1995. Leptons are combined with opposite sign D_s^- candidates reconstructed in seven different decay modes as evidence of semileptonic B_s^0 decays. Criteria designed to ensure precise proper time reconstruction select 277 $D_s^- \ell^+$ combinations. The initial state of these B_s^0 candidates is determined using an algorithm optimized to efficiently utilise the tagging information available for each event. The limit at 95% confidence level on the $B_s^0 \bar{B}_s^0$ oscillation frequency is $\Delta m_s > 6.6\ ps^{-1}$. The same data is used to update the measurement of the B_s^0 lifetime, $\tau_s = 1.54\ ^{+0.14}_{-0.13}\ (stat) \pm 0.04\ (syst)\ ps$.

The ALEPH Collaboration

D. Buskulic, I. De Bonis, D. Decamp, P. Ghez, C. Goy, J.-P. Lees, A. Lucotte, M.-N. Minard, P. Odier, B. Pietrzyk

Laboratoire de Physique des Particules (LAPP), IN²P³-CNRS, 74019 Annecy-le-Vieux Cedex, France

M.P. Casado, M. Chmeissani, J.M. Crespo, M. Delfino,[12] I. Efthymiopoulos,[1] E. Fernandez, M. Fernandez-Bosman, Ll. Garrido,[15] A. Juste, M. Martinez, S. Orteu, A. Pacheco, C. Padilla, A. Pascual, J.A. Perlas, I. Riu, F. Sanchez, F. Teubert

Institut de Fisica d'Altes Energies, Universitat Autonoma de Barcelona, 08193 Bellaterra (Barcelona), Spain[7]

A. Colaleo, D. Creanza, M. de Palma, G. Gelao, M. Girone, G. Iaselli, G. Maggi,[3] M. Maggi, N. Marinelli, S. Nuzzo, A. Ranieri, G. Raso, F. Ruggieri, G. Selvaggi, L. Silvestris, P. Tempesta, G. Zito

Dipartimento di Fisica, INFN Sezione di Bari, 70126 Bari, Italy

X. Huang, J. Lin, Q. Ouyang, T. Wang, Y. Xie, R. Xu, S. Xue, J. Zhang, L. Zhang, W. Zhao

Institute of High-Energy Physics, Academia Sinica, Beijing, The People's Republic of China[8]

R. Alemany, A.O. Bazarko, G. Bonvicini,[23] M. Cattaneo, P. Comas, P. Coyle, H. Drevermann, R.W. Forty, M. Frank, R. Hagelberg, J. Harvey, P. Janot, B. Jost, E. Kneringer, J. Knobloch, I. Lehraus, G. Lutters, E.B. Martin, P. Mato, A. Minten, R. Miquel, Ll.M. Mir,[2] L. Moneta, T. Oest,[20] J.R. Pater,[27] J.-F. Pusztaszeri, F. Ranjard, P. Rensing,[34] L. Rolandi, D. Schlatter, M. Schmelling,[24] O. Schneider, W. Tejessy, I.R. Tomalin, A. Venturi, H. Wachsmuth, A. Wagner, T. Wildish

European Laboratory for Particle Physics (CERN), 1211 Geneva 23, Switzerland

Z. Ajaltouni, A. Barrès, C. Boyer, A. Falvard, P. Gay, C . Guicheney, P. Henrard, J. Jousset, B. Michel, S. Monteil, J-C. Montret, D. Pallin, P. Perret, F. Podlyski, J. Proriol, J.-M. Rossignol

Laboratoire de Physique Corpusculaire, Université Blaise Pascal, IN²P³-CNRS, Clermont-Ferrand, 63177 Aubière, France

T. Fearnley, J.B. Hansen, J.D. Hansen, J.R. Hansen, P.H. Hansen, B.S. Nilsson, A. Wäänänen

Niels Bohr Institute, 2100 Copenhagen, Denmark[9]

A. Kyriakis, C. Markou, E. Simopoulou, I. Siotis, A. Vayaki, K. Zachariadou

Nuclear Research Center Demokritos (NRCD), Athens, Greece

A. Blondel, G. Bonneaud, J.C. Brient, P. Bourdon, A. Rougé, M. Rumpf, A. Valassi,[6] M. Verderi, H. Videau[21]

Laboratoire de Physique Nucléaire et des Hautes Energies, Ecole Polytechnique, IN²P³-CNRS, 91128 Palaiseau Cedex, France

D.J. Candlin, M.I. Parsons

Department of Physics, University of Edinburgh, Edinburgh EH9 3JZ, United Kingdom[10]

E. Focardi,[21] G. Parrini

Dipartimento di Fisica, Università di Firenze, INFN Sezione di Firenze, 50125 Firenze, Italy

M. Corden, C. Georgiopoulos, D.E. Jaffe

Supercomputer Computations Research Institute, Florida State University, Tallahassee, FL 32306-4052, USA[13,14]

A. Antonelli, G. Bencivenni, G. Bologna,[4] F. Bossi, P. Campana, G. Capon, D. Casper, V. Chiarella, G. Felici, P. Laurelli, G. Mannocchi,[5] F. Murtas, G.P. Murtas, L. Passalacqua, M. Pepe-Altarelli

Laboratori Nazionali dell'INFN (LNF-INFN), 00044 Frascati, Italy

L. Curtis, S.J. Dorris, A.W. Halley, I.G. Knowles, J.G. Lynch, V. O'Shea, C. Raine, P. Reeves, J.M. Scarr, K. Smith, A.S. Thompson, F. Thomson, S. Thorn, R.M. Turnbull

Department of Physics and Astronomy, University of Glasgow, Glasgow G12 8QQ,United Kingdom[10]

U. Becker, C. Geweniger, G. Graefe, P. Hanke, G. Hansper, V. Hepp, E.E. Kluge, A. Putzer, B. Rensch, M. Schmidt, J. Sommer, H. Stenzel, K. Tittel, S. Werner, M. Wunsch

Institut für Hochenergiephysik, Universität Heidelberg, 69120 Heidelberg, Fed. Rep. of Germany[16]

D. Abbaneo, R. Beuselinck, D.M. Binnie, W. Cameron, P.J. Dornan, A. Moutoussi, J. Nash, J.K. Sedgbeer, A.M. Stacey, M.D. Williams

Department of Physics, Imperial College, London SW7 2BZ, United Kingdom[10]

G. Dissertori, P. Girtler, D. Kuhn, G. Rudolph

Institut für Experimentalphysik, Universität Innsbruck, 6020 Innsbruck, Austria[18]

A.P. Betteridge, C.K. Bowdery, P. Colrain, G. Crawford, A.J. Finch, F. Foster, G. Hughes, T. Sloan, M.I. Williams

Department of Physics, University of Lancaster, Lancaster LA1 4YB, United Kingdom[10]

A. Galla, A.M. Greene, K. Kleinknecht, G. Quast, B. Renk, E. Rohne, H.-G. Sander, P. van Gemmeren C. Zeitnitz

Institut für Physik, Universität Mainz, 55099 Mainz, Fed. Rep. of Germany[16]

J.J. Aubert,[21] A.M. Bencheikh, C. Benchouk, A. Bonissent,[21] G. Bujosa, D. Calvet, J. Carr, C. Diaconu, F. Etienne, N. Konstantinidis, P. Payre, D. Rousseau, M. Talby, A. Sadouki, M. Thulasidas, K. Trabelsi

Centre de Physique des Particules, Faculté des Sciences de Luminy, IN^{2}P^3-CNRS, 13288 Marseille, France

M. Aleppo, F. Ragusa[21]

Dipartimento di Fisica, Università di Milano e INFN Sezione di Milano, 20133 Milano, Italy

I. Abt, R. Assmann, C. Bauer, W. Blum, H. Dietl, F. Dydak,[21] G. Ganis, C. Gotzhein, K. Jakobs, H. Kroha, G. Lütjens, G. Lutz, W. Männer, H.-G. Moser, R. Richter, A. Rosado-Schlosser, S. Schael, R. Settles, H. Seywerd, R. St. Denis, W. Wiedenmann, G. Wolf

Max-Planck-Institut für Physik, Werner-Heisenberg-Institut, 80805 München, Fed. Rep. of Germany[16]

J. Boucrot, O. Callot, A. Cordier, M. Davier, L. Duflot, J.-F. Grivaz, Ph. Heusse, M. Jacquet, D.W. Kim,[19] F. Le Diberder, J. Lefrançois, A.-M. Lutz, I. Nikolic, H.J. Park,[19] I.C. Park,[19] M.-H. Schune, S. Simion, J.-J. Veillet, I. Videau

Laboratoire de l'Accélérateur Linéaire, Université de Paris-Sud, IN^{2}P^3-CNRS, 91405 Orsay Cedex, France

P. Azzurri, G. Bagliesi, G. Batignani, S. Bettarini, C. Bozzi, G. Calderini, M. Carpinelli, M.A. Ciocci, V. Ciulli, R. Dell'Orso, R. Fantechi, I. Ferrante, L. Foà,[1] F. Forti, A. Giassi, M.A. Giorgi, A. Gregorio, F. Ligabue, A. Lusiani, P.S. Marrocchesi, A. Messineo, F. Palla, G. Rizzo, G. Sanguinetti, A. Sciabà, P. Spagnolo, J. Steinberger, R. Tenchini, G. Tonelli,[26] C. Vannini, P.G. Verdini, J. Walsh

Dipartimento di Fisica dell'Università, INFN Sezione di Pisa, e Scuola Normale Superiore, 56010 Pisa, Italy

G.A. Blair, L.M. Bryant, F. Cerutti, J.T. Chambers, Y. Gao, M.G. Green, T. Medcalf, P. Perrodo, J.A. Strong, J.H. von Wimmersperg-Toeller

Department of Physics, Royal Holloway & Bedford New College, University of London, Surrey TW20 OEX, United Kingdom[10]

D.R. Botterill, R.W. Clifft, T.R. Edgecock, S. Haywood, P. Maley, P.R. Norton, J.C. Thompson, A.E. Wright

Particle Physics Dept., Rutherford Appleton Laboratory, Chilton, Didcot, Oxon OX11 OQX, United Kingdom[10]

B. Bloch-Devaux, P. Colas, S. Emery, W. Kozanecki, E. Lançon, M.C. Lemaire, E. Locci, B. Marx, P. Perez, J. Rander, J.-F. Renardy, A. Roussarie, J.-P. Schuller, J. Schwindling, A. Trabelsi, B. Vallage

CEA, DAPNIA/Service de Physique des Particules, CE-Saclay, 91191 Gif-sur-Yvette Cedex, France[17]

S.N. Black, J.H. Dann, R.P. Johnson, H.Y. Kim, A.M. Litke, M.A. McNeil, G. Taylor

Institute for Particle Physics, University of California at Santa Cruz, Santa Cruz, CA 95064, USA[22]

C.N. Booth, R. Boswell, C.A.J. Brew, S. Cartwright, F. Combley, A. Koksal, M. Letho, W.M. Newton, J. Reeve, L.F. Thompson

Department of Physics, University of Sheffield, Sheffield S3 7RH, United Kingdom[10]

A. Böhrer, S. Brandt, V. Büscher, G. Cowan, C. Grupen, J. Minguet-Rodriguez, F. Rivera,[25] P. Saraiva, L. Smolik, F. Stephan,

Fachbereich Physik, Universität Siegen, 57068 Siegen, Fed. Rep. of Germany[16]

M. Apollonio, L. Bosisio, R. Della Marina, G. Giannini, B. Gobbo, G. Musolino

Dipartimento di Fisica, Università di Trieste e INFN Sezione di Trieste, 34127 Trieste, Italy

J. Rothberg, S. Wasserbaech

Experimental Elementary Particle Physics, University of Washington, WA 98195 Seattle, U.S.A.

S.R. Armstrong, L. Bellantoni,[30] P. Elmer, Z. Feng,[31] D.P.S. Ferguson, Y.S. Gao,[32] S. González, J. Grahl, T.C. Greening, J.L. Harton,[28] O.J. Hayes, H. Hu, P.A. McNamara III, J.M. Nachtman, W. Orejudos, Y.B. Pan, Y. Saadi, M. Schmitt, I.J. Scott, V. Sharma,[29] A.M. Walsh,[33] Sau Lan Wu, X. Wu, J.M. Yamartino, M. Zheng, G. Zobernig

Department of Physics, University of Wisconsin, Madison, WI 53706, USA[11]

1 Introduction

Oscillations in the neutral B meson system are a well established phenomenon and the B_d^0 oscillation frequency is now rather precisely measured [1]. The observed B_d^0 and $\bar{B}_d^0$ states are linear combinations of the two mass eigenstates. The same holds for B_s^0 and $\bar{B}_s^0$ mesons. For an initially pure B^0 state, the probability density of observing the decay of a $\bar{B}^0$ at time t is

$$\mathcal{P}_m = \frac{1}{\tau} \, e^{-t/\tau} \, \frac{1 - \cos(\Delta m t)}{2}, \tag{1}$$

the m index standing for "mixed"; τ is the neutral B meson lifetime, t is the proper time and Δm is the mass difference of the two mass eigenstates. Similarly, the probability density of observing the decay of a B^0 at time t is

$$\mathcal{P}_u = \frac{1}{\tau} \, e^{-t/\tau} \, \frac{1 + \cos(\Delta m t)}{2}, \tag{2}$$

where the u index stands for "unmixed". These expressions are obtained assuming equal lifetimes for the two states and neglecting CP violation. Within the Standard Model (SM), the mass differences for the $B_s^0 \bar{B}_s^0$ and the $B_d^0 \bar{B}_d^0$ systems occur due to the presence of box diagrams for which top quark exchange dominates. The mass differences depend on the Cabibbo–Kobayashi–Maskawa (CKM) matrix elements, on the top quark mass and on QCD correction factors, both perturbative and non−perturbative. These QCD factors are not precisely computed but their ratios for the B_d^0 and B_s^0 have less uncertainty allowing the ratio $\Delta m_s/\Delta m_d$ and the CKM matrix elements to be linked with higher accuracy;

$$\frac{\Delta m_s}{\Delta m_d} = \frac{m_s}{m_d} \left| \frac{V_{ts}}{V_{td}} \right|^2 \xi^2 \frac{\hat{\eta}_s}{\hat{\eta}_d}. \tag{3}$$

The $\hat{\eta}_s$ and $\hat{\eta}_d$ correction factors for the B_s^0 and the B_d^0 are identical [2]. The ratio of the hadronic matrix elements for the B_d^0 and the B_s^0 is estimated to be $\xi = 1.16 \pm 0.10$ [3]. Therefore, measurements of Δm_s and Δm_d will constrain the ratio of the CKM matrix elements V_{ts} and V_{td}.

The oscillations of the B_s^0 meson are an area of intense study at LEP [4, 5, 6, 7, 8]. All of these previous studies use partially reconstructed semileptonic B decays to reconstruct the decay length and identify the final state of the B meson and a variety of methods to identify or "tag" the initial state of the B meson. These studies generally do not differentiate between leptons from the B_s^0 and other b hadron decays and are therefore directly sensitive to the relative fractions of b quarks that hadronize into B_d^0, B^-, B_s^0 and b baryons.

This paper presents a study of the oscillation frequency of the $B_s^0 \bar{B}_s^0$ system using $B_s^0 \rightarrow D_s^- \ell^+ \nu X$ semileptonic decays[1]. The B_s^0 candidate selection yields a sample of 277 reconstructed $D_s^- \ell^+$ combinations, indicative of semileptonic B_s^0 decays, with a much higher B_s^0 purity and improved proper time resolution than the previous Δm_s analyses. In order to fully exploit this small sample of events, a method has been developed which optimally combines information from up to three different initial state tags. The mixed or unmixed state of the event is determined by comparing the charge of the lepton of the $D_s^\mp \ell^\pm$ combination and the tagging of the production state of the B_s^0 or $\bar{B}_s^0$ meson.

2 The ALEPH detector

The ALEPH detector and its performance are described in detail elsewhere [9, 10] and only a brief overview of the apparatus is given here. A high resolution vertex detector (VDET) consisting of two

---

[1]In this paper charge conjugate modes are always implied and "lepton" (ℓ^+) refers to electrons and muons.

layers of double-sided silicon microstrip detectors surrounds the beam pipe. The inner layer is 6.5 cm from the beam axis and covers 85% of the solid angle and the outer layer is at an average radius of 11.3 cm and covers 69%. The spatial resolution for the $r\phi$ and z projections (transverse to and along the beam axis, respectively) is 12 μm at normal incidence. The vertex detector is surrounded by a drift chamber with eight coaxial wire layers with an outer radius of 26 cm and by a time projection chamber (TPC) that measures up to 21 three–dimensional points per track at radii between 30 cm and 180 cm. These detectors are immersed in an axial magnetic field of 1.5 T and together measure the momenta of charged particles with a resolution $\sigma(p)/p = 6 \times 10^{-4} p_{\mathrm{T}} \oplus 0.005$ (p_{T} in GeV/c). The resolution of the three–dimensional impact parameter in the transverse and longitudinal view for tracks having information from all tracking detectors and two VDET hits can be parameterized as $\sigma = 25\mu\mathrm{m} + 95\mu\mathrm{m}/p$ (p in GeV/c). The TPC also provides up to 338 measurements of the specific ionization of a charged track (dE/dx). The TPC is surrounded by a lead/proportional–chamber electromagnetic calorimeter segmented into $0.9° \times 0.9°$ projective towers and read out in three sections in depth, with energy resolution $\sigma(E)/E = 0.18/\sqrt{E} + 0.009$ (E in GeV). The iron return yoke of the magnet is instrumented with streamer tubes to form a hadron calorimeter, with a thickness of over 7 interaction lengths and is surrounded by two additional double-layers of streamer tubes to aid in muon identification. An algorithm combines all these measurements to provide a determination of the energy flow [10] with an uncertainty on the measurable total energy of $\sigma(E) = 0.6\sqrt{E/\mathrm{GeV}} + 0.6$ GeV.

The selection of hadronic events is based on charged tracks and is described elsewhere [11]. The interaction point is reconstructed on an event-by-event basis using the constraint of the average beam spot position and envelope [12]. The average resolution is 85 μm for Z $\rightarrow b\bar{b}$ events, projected along the sphericity axis of the event.

3 $\mathrm{B}^0_{\mathrm{s}}$ candidate reconstruction

This analysis uses approximately four million hadronic Z decays recorded by the ALEPH detector from 1991 to 1995 at centre of mass energies close to the Z mass. Monte Carlo samples of fully simulated Z $\rightarrow q\bar{q}$ and Z $\rightarrow b\bar{b}$ decays are used in this study. The Monte Carlo generator is based on JETSET 7.3 [13] with updated branching ratios, and the Körner-Schuler model [14] is used for semileptonic b hadron decays.

The $\mathrm{B}^0_{\mathrm{s}}$ candidate selection is identical to that used for the previous ALEPH measurement of the $\mathrm{B}^0_{\mathrm{s}}$ lifetime [15]. The $\mathrm{B}^0_{\mathrm{s}}$ is reconstructed in the semileptonic decay mode $\mathrm{B}^0_{\mathrm{s}} \rightarrow \mathrm{D}^-_{\mathrm{s}} \ell^+ \nu X$ and the $\mathrm{D}^-_{\mathrm{s}}$ is reconstructed in two semileptonic modes involving a ϕ resonance and five hadronic decay modes. The calculated yields of signal and background are given in Table 1. The $\mathrm{B}^0_{\mathrm{s}} \rightarrow \mathrm{D}^-_{\mathrm{s}} \ell^+ \nu X$ signal comprises the two decays $\mathrm{B}^0_{\mathrm{s}} \rightarrow \mathrm{D}^{*-}_{\mathrm{s}} \ell^+ \nu$ and $\mathrm{B}^0_{\mathrm{s}} \rightarrow \mathrm{D}^-_{\mathrm{s}} \ell^+ \nu$, as $\mathrm{D}^{*-}_{\mathrm{s}} \rightarrow \mathrm{D}^-_{\mathrm{s}} \gamma$ and $\mathrm{D}^{*-}_{\mathrm{s}} \rightarrow \mathrm{D}^-_{\mathrm{s}} \pi^0$ decays dominate [16, 17] and higher order $\bar{c}s$ resonances decay to $\mathrm{D}^{(*)}\mathrm{K}$ final states.

In this paper, "$\bar{\mathrm{B}} \rightarrow \mathrm{D}^{(*)-}_{\mathrm{s}} \mathrm{D}^{(*)} X$" denotes all spectator decays of b hadrons in which the virtual W^- produces a $\mathrm{D}^-_{\mathrm{s}}$ and either the remaining c quark decays semileptonically or, for the $\bar{\mathrm{B}}^0_{\mathrm{s}} \rightarrow \mathrm{D}^{(*)-}_{\mathrm{s}} \mathrm{D}^{(*)+}_{\mathrm{s}} X$ component of the background, one of the D_{s} mesons decays semileptonically. As shown in Table 1, the $\mathrm{B}^0_{\mathrm{s}}$ fraction is larger than 60%, in contrast to approximately 10% in previous $\mathrm{B}^0_{\mathrm{s}}\bar{\mathrm{B}}^0_{\mathrm{s}}$ oscillation studies [4, 5, 6, 7, 8].

For the combinatorial background studies, two regions in the reconstructed $\mathrm{D}^-_{\mathrm{s}}$ mass for the hadronic modes or ϕ mass for the semileptonic modes are defined. The first region contains unlike-sign candidates, $\mathrm{D}^{\pm}_{\mathrm{s}} \ell^{\mp}$ ($\phi\ell^{\pm}\ell^{\mp}$), and extends from 2.05 to 2.30 (1.021 to 1.120) GeV/c^2. The second region contains the like–sign candidates, $\mathrm{D}^{\pm}_{\mathrm{s}} \ell^{\pm}$ ($\phi\ell^{\pm}\ell^{\pm}$), and extends from 1.95 to 2.30 (0.997 to 1.120) GeV/c^2. These two regions will be collectively referred to as "sidebands".

D_s^- decay mode	$D_s^- \ell^+ \nu X$ signal	$D_s^{(*)-} D^{(*)} X$ background	Combinatorial background	Total per mode
$\phi \pi^-$	47.8	4.7	8.5 ± 1.0	61
$K^{*0} K^-$	64.7	5.9	30.1 ± 2.9	102
$K_s^0 K^-$	13.0	1.1	6.9 ± 1.4	21
$\phi \pi^+ \pi^- \pi^-$	14.8	1.3	14.8 ± 2.4	31
$K^{*0} K^{*-}$	11.5	1.0	5.5 ± 1.2	18
$\phi e^- \nu$	20.2	1.1	8.7 ± 1.6	30
$\phi \mu^- \nu$	9.6	0.5	3.9 ± 1.1	14
TOTAL	181.6	15.6	78.5 ± 4.7	277

Table 1: The estimated contributions to the total yield for each decay mode. The estimated contribution of 1.3 $D^- \to K^{*0} \pi^-$ events to the $K^{*0} K^-$ mode is not shown in the table but is included in the totals.

The B_s^0 momentum is computed from the reconstructed $D_s^- \ell^+$ momentum $p(D_s^- \ell^+)$ and the neutrino energy estimated using a missing energy technique [18]; it is corrected for a bias due to a slight dependence of the calculated missing energy on $p(D_s^- \ell^+)$. This small correction (typically 4%) is parametrized as

$$p = a + b \times p(uncorrected),\qquad(4)$$

where $a = 3.1 \pm 0.2$ GeV/c and $b = 0.873 \pm 0.006$ are determined from Monte Carlo. The measured proper time of the B_s^0 is then obtained as

$$t_m = \frac{m_s L}{p},\qquad(5)$$

where $m_s = 5375 \pm 6$ MeV/c^2 [16] is the B_s^0 mass and L is the reconstructed decay length, computed as the projection on $p(D_s^- \ell^+)$ of the distance between the primary and the $D_s^- \ell^+$ vertices.

The resolution on the proper time is calculated on an event-by-event basis as

$$\sigma_t^2 = \left(\frac{m_s}{p}\right)^2 \times \left((S_L \sigma_L)^2 + \left(\frac{L \sigma_p}{p}\right)^2\right),\qquad(6)$$

where $\sigma_p = 3.1 \pm 0.4$ GeV/c is the uncertainty in p determined from Monte Carlo and σ_L is the uncertainty in the reconstructed decay length calculated for each $D_s^- \ell^+$ candidate as described in [15]. The scale factor S_L on the decay length uncertainty comprises two effects. From Monte Carlo studies the decay length uncertainty is underestimated by 1.13 ± 0.10 and 1.35 ± 0.10 for the D_s^- hadronic and semileptonic decay modes, respectively. The correction factor is larger for the semileptonic decay modes because of the increased uncertainty on the D_s^- direction due to the missing neutrino. The widths of the distributions of L/σ_L for $L < 0$ of data and Monte Carlo are compared for samples enriched in zero-lifetime events [15] to obtain a global correction factor of 1.05 ± 0.03. These effects are combined to obtain $S_L = 1.19 \pm 0.11$ and $S_L = 1.42 \pm 0.11$ for the hadronic and semileptonic decay modes, respectively.

Monte Carlo simulation shows that the average B_s^0 decay length resolution is 210 μm for the hadronic D_s^- decays, and the B_s^0 decay length resolution is approximately 20% worse for the semileptonic D_s^- decays due to the unobserved neutrino which increases the uncertainty in the

3

reconstructed D_s^- direction. The distribution of the calculated proper time resolution for the 277 $D_s^- \ell^+$ combinations is shown in Figure 1(a).

Update of the B_s^0 lifetime measurement

The B_s^0 lifetime is measured to be $1.54 \, ^{+0.14}_{-0.13} \, (stat) \pm 0.04 \, (syst)$ ps with the additional data included in this analysis. This result supersedes the previous measurement $(1.59 \, ^{+0.17}_{-0.15} \, (stat) \pm 0.03 \, (syst)$ ps) presented in reference [15], which contains a description of the method and of the individual contributions to the systematic uncertainty listed in Table 2. The proper time distribution and fit are shown in Figure 1(b).

Source	Uncertainty (ps)	
Combinatorial background	+0.013	−0.024
$\bar{B} \to D_s^{(*)-} D^{(*)} X$ background	+0.023	−0.015
$B \to D_s^- X_s \ell^+ \nu$ background	+0.000	−0.009
Proper time resolution parametrization bias	+0.008	−0.008
Parametrization of proper time resolution	+0.015	−0.015
$L_{D_s^-}/\sigma(L_{D_s^-}) > -0.5$ bias	+0.010	−0.010
B_s^0 boost resolution	+0.010	−0.010
Other	+0.007	−0.004
Total in quadrature	+0.036	−0.037

Table 2: The components of the estimated systematic uncertainty on the measured B_s^0 lifetime. For the $\bar{B} \to D_s^{(*)-} D^{(*)} X$ background, the branching ratios $Br(\bar{B} \to D_s^- X) = 0.1046 \pm 0.0073$ [19, 20] and $Br(b \to c \to \ell) = 0.0822 \pm 0.0046$ [21] are used as in [15].

4 Initial state identification

Identification of the initial state of the neutral B meson begins by dividing a $Z \to b\bar{b}$ event into hemispheres using the thrust axis to separate the products of the b and the $\bar{b}$ as shown schematically in Figure 2. Previous studies of time dependent neutral B meson oscillations have either identified the initial state of the B^0 or $\bar{B}^0$ by the charge of a lepton in the hemisphere opposite to the partially reconstructed B [4, 8, 22], by the net charge of the jet in the opposite hemisphere [23], by a linear combination of the charge of the jets in both hemispheres [5, 24], by a combination of the opposite hemisphere lepton and jet charges [7, 25] or by a combination of the charge of a fragmentation kaon and the opposite hemisphere jet charge [6]. All these studies place requirements on the lepton transverse momentum with respect to its jet or on the magnitude of the jet charge in order to reduce the fraction of incorrectly tagged events. Rather than decreasing the statistical precision by rejecting events and then treating the selected events on equal footing, an algorithm has been developed [26] which utilises the tagging information available in each $D_s^- \ell^+$ event.

The usefulness of such an algorithm can be demonstrated using the opposite hemisphere jet charge. Both the sign and the magnitude of the jet charge contain information on the quark initiating the jet. For example, the larger the magnitude of a positively-signed jet charge, the more likely it is that a $\bar{b}$ quark initiated the jet. In the rest of this paper, quantities such as the jet charge, which can

4

improve the ability of a tag to determine the initial state quark will be referred to as "discriminating variables". The method proceeds in three related steps:

1. Identification of a set of tags,

2. Classification of each event based on the available tags and discriminating variables, and

3. Creation of the event-by-event mistag probability based on the tags and the discriminating variables.

These steps are described in detail in the following three sections.

4.1 Tag description

The tagging algorithm relies upon three basic tags which are described below and shown schematically in Figure 2.

1. **Lepton tag:** A lepton with momentum greater than 3 GeV/c and passing standard identification requirements [27] (the electron candidates are kept even if the dE/dx information is not available) is searched for in the hemisphere opposite to the $D_s^-\ell^+$ candidate. The lepton candidate with the highest momentum is selected when more than one candidate is found. The sign of the lepton tags the nature of the initial b quark in the opposite hemisphere and thus identifies the initial state of the B_s^0 in the $D_s^-\ell^+$ hemisphere (Figure 2). There is no cut on the lepton transverse momentum with respect to the jet axis and a significant contribution from the cascade decay, $b \to c \to \ell$, is expected at low transverse momentum. This tag has the highest purity but has a relatively low efficiency due to the b semileptonic branching ratio.

2. **Fragmentation kaon tag:** During the fragmentation process, a rather energetic K^+ carrying an $\bar{s}$ quark can be produced concurrently with the B_s^0 ($\bar{b}s$) [28]. Identification of such a charged kaon in the $D_s^-\ell^+$ hemisphere tags the initial B_s^0 state. The fragmentation kaon candidate is defined as the highest momentum track within 45 degrees of the $D_s^-\ell^+$ direction satisfying $|\chi_K| < 2$ and $d/\sigma_d < 3$. The dE/dx estimator χ_K is the difference between the measured and expected ionization for the kaon hypothesis normalised in terms of the expected resolution, and d is the three-dimensional impact parameter of the track with respect to the primary vertex. This tag is less pure than the lepton tag but more efficient.

3. **Opposite hemisphere jet charge tag:** The jet charge for the opposite hemisphere is defined as

$$Q_\circ \equiv \frac{\sum_i q_i |p_\parallel^i|^\kappa}{\sum_i |p_\parallel^i|^\kappa}, \tag{7}$$

where the sum is over all charged particles in the hemisphere opposite to the $D_s^-\ell^+$ candidate, $p_\parallel^i$ is the momentum of the ith track projected on the thrust axis, q_i its charge and $\kappa = 0.5$. The sign of $Q_\circ$ tags the initial state of the b in the opposite hemisphere. This is the most efficient of the three tags but has the lowest purity.

4.2 Class definitions and discriminating variables.

The B_s^0 candidate events are sorted into seven exclusive classes based on the availability of the three tags and the associated discriminating variables.

- **Class 1** The sign of Q_o ($\equiv S(Q_o)$) tags the initial B_s^0 or $\bar{B}_s^0$ state. The discriminating variables in this class are the magnitude of Q_o and $S(Q_o) \times Q_s$, where Q_s is the jet charge of the same hemisphere as the $D_s^- \ell^+$, excluding the tracks of the $D_s^- \ell^+$ candidate and using $\kappa = 1.0$. This definition of Q_s (ideally the jet charge of a jet initiated by an s or $\bar{s}$ quark) differs from previous studies [5, 24] which formed a same hemisphere jet charge that included the charged tracks of the B^0 candidate. Monte Carlo studies show that $\kappa = 1.0$ slightly improves the discriminating power of Q_s with respect to $\kappa = 0.5$ [5] and $\kappa = 0$ [24] .

- **Class 2** The sign of the fragmentation kaon ($\equiv S(K)$) tags the initial B_s^0 or $\bar{B}_s^0$ state. The discriminating variables are $S(K) \times Q_o$, $S(K) \times Q_s$, χ_π and Z_K where χ_π is the dE/dx estimator for the fragmentation kaon under the pion hypothesis and

$$Z_K \equiv \frac{p_K}{E_{beam} - E_{B_s^0}}, \tag{8}$$

  where p_K is the momentum of the fragmentation kaon candidate and $E_{B_s^0}$ is the reconstructed B_s^0 energy calculated from the reconstructed B_s^0 momentum (section 3) and the B_s^0 mass [16]. The fragmentation kaon should carry a large fraction of the available energy since it is the first particle produced in the hadronization chain [29].

- **Class 3** In this class the sign of the opposite hemisphere lepton tags the initial B_s^0 or $\bar{B}_s^0$ state and the discriminating variables are $S(\ell) \times Q_o$, $S(\ell) \times Q_s$ and $p_T(\ell)$, the transverse momentum of the lepton with respect to the jet axis with the lepton removed from the jet [27].

- **Classes 4 and 5** The maximum information is available in these two classes: the jet charges, the fragmentation kaon and the opposite hemisphere lepton. The lepton sign is used to tag the initial B_s^0 or $\bar{B}_s^0$ state and the discriminating variables are χ_π, Z_K, $S(\ell) \times Q_o$, $S(\ell) \times Q_s$ and $p_T(\ell)$. For class 4 the fragmentation kaon tag and the opposite hemisphere lepton tag agree on the initial B_s^0 or $\bar{B}_s^0$ state whereas for class 5 they disagree.

- **Classes 6 (7)** This class is similar to the class 1 (3) except that the same hemisphere jet charge Q_s information is not available. This situation occurs when the only charged tracks in the $D_s^- \ell^+$ hemisphere belong to the $D_s^- \ell^+$ candidate.

As indicated in Figure 2, the opposite hemisphere lepton is included in the calculation of Q_o for classes 3, 4, 5 and 7. The fragmentation kaon is included in the calculation of Q_s for classes 2, 4 and 5. The correlations induced by this procedure between $p_T(\ell)$ and Q_o or Z_K and Q_s are taken into account in the formulation of the mistag probability as described in the next section.

The method described tags all 277 $D_s^- \ell^+$ candidates of which 145 or 53% are tagged as "mixed". The populations of each class in data and Monte Carlo are given in Table 3.

4.3 Calculation of the event-by-event mistag probability

In most of the previous analyses [4, 5, 6, 7, 8] the additional information provided by the magnitude of the jet charge or the lepton transverse momentum was neglected[2], and the mistag probability was

---

[2]Information from the jet charge magnitude was used in [8].

Class	Tag	Discriminating variables					Events observed	Fraction observed (%)	Fraction in Monte Carlo (%)
1	$Q_\circ$	$S(Q_\circ) \times Q_s$	$\lvert Q_\circ \rvert$				114	41	35.1 ± 1.0
2	Kaon	$S(K) \times Q_s$	$S(K) \times Q_\circ$		Z_K	χ_π	97	35	40.3 ± 1.0
3	Lepton	$S(\ell) \times Q_s$	$S(\ell) \times Q_\circ$	$p_T(\ell)$			27	10	9.6 ± 0.6
4	Lepton	$S(\ell) \times Q_s$	$S(\ell) \times Q_\circ$	$p_T(\ell)$	Z_K	χ_π	17	6	7.0 ± 0.5
5	Lepton	$S(\ell) \times Q_s$	$S(\ell) \times Q_\circ$	$p_T(\ell)$	Z_K	χ_π	13	5	4.9 ± 0.4
6	$Q_\circ$	$\lvert Q_\circ \rvert$					7	3	2.6 ± 0.3
7	Lepton	$S(\ell) \times Q_\circ$	$p_T(\ell)$				2	1	0.5 ± 0.1

Table 3: The tag and discrimating variables for each class are listed in columns 2 and 3, respectively. The number and fraction of events in the data, and the fraction of events in the $B_s^0 \to D_s^- \ell^+ \nu X$ Monte Carlo are shown in columns 4, 5 and 6, respectively.

simply taken as the mistag fraction

$$\eta \equiv \frac{N_{wrong}}{N_{wrong} + N_{right}}, \tag{9}$$

where N_{right} (N_{wrong}) is the number of B_s^0 or $\bar{B}_s^0$ whose initial state is correctly (incorrectly) determined by the tagging algorithm. For a given class with a set of discriminating variables $\{x_i\}$ and a tag as described in the previous section[3] the optimal separation between right and wrong tag events is achieved with the following definition of the event-by-event mistag probability [26]

$$X_{eff}(\{x_i\}) \equiv \frac{\eta w(\{x_i\})}{(1-\eta)r(\{x_i\}) + \eta w(\{x_i\})}, \tag{10}$$

where η is the mistag fraction of that class, and $r(\{x_i\})$ and $w(\{x_i\})$ are the multi–dimensional probability density distributions for events in which the tag identifies the right and wrong initial B_s^0 or $\bar{B}_s^0$ state, respectively. Although the mistag probability formulated in this way includes the correlations between the discriminating variables, it is difficult to accurately parametrize r and w as prohibitive amounts of Monte Carlo are required to adequately populate the multi–dimensional space. In practice the multi–dimensional distributions are approximated by the product of one–dimensional probability density distributions

$$x_{eff}(\{x_i\}) \equiv \frac{\eta w_1(x_1) w_2(x_2) \cdots}{(1-\eta)r_1(x_1)r_2(x_2)\cdots + \eta w_1(x_1)w_2(x_2)\cdots}, \tag{11}$$

where $r_i(x_i)$ and $w_i(x_i)$ are the probability density distributions for discriminating variable x_i.

If all discriminating variables in the class are independent, then x_{eff} of Equation 11 would be the event-by-event mistag probability. However, in the presence of correlations (which is the case for the discriminating variables in the classes defined in the previous section), the event-by-event mistag probability is computed as

$$X_{eff}(x_{eff}) \equiv \frac{\eta W(x_{eff})}{(1-\eta)R(x_{eff}) + \eta W(x_{eff})}, \tag{12}$$

---

[3]For example, in class 3, $\{x_i\} = \{x_1, x_2, x_3\}$ with $x_1 = p_T(\ell)$, $x_2 = S(\ell) \times Q_s$ and $x_3 = S(\ell) \times Q_\circ$, and the tag is the charge of the opposite hemisphere lepton.

where $R(x_{eff})$ and $W(x_{eff})$ are the probability distributions of x_{eff} for the the right- and wrong-tags, respectively. Equation 12 is just a special case of Equation 10 where only a single discriminating variable x_{eff} is considered for a class.

The distributions of $r_i(x_i)$ and $w_i(x_i)$ for each discriminating variable, as well as the distributions of $R(x_{eff})$ and $W(x_{eff})$, are determined for each class from simulated $B_s^0 \to D_s^- \ell^+ \nu X$ decays with $\Delta m_s = 10$ ps^{-1}, $\Delta m_d = 0.5$ ps^{-1}, and a lifetime of 1.5 ps for all b hadrons. These Monte Carlo events are analyzed as the data and represent approximately 20 times the number of events in the data. As an example, Figure 3 shows the unnormalised distributions of r_i and w_i of each of the discriminating variables of class 3, as well as the relationship between X_{eff} and these variables.

An additional probability distribution $B(x_{eff})$ is determined from the "sidebands" in the data for each class and decay mode to represent the distribution of x_{eff} for the background. An event-by-event background fraction is calculated as

$$Z_{eff}(x_{eff}) \equiv \frac{\zeta B(x_{eff})}{(1-\eta) R(x_{eff}) + \eta W(x_{eff})}, \tag{13}$$

where the relative background to signal rate

$$\zeta \equiv N_{Background}/N_{Signal} \tag{14}$$

is determined for each decay mode from the data (Table 1).

The distributions of $R(x_{eff})$, $W(x_{eff})$ and $B(x_{eff})$ are compared with the distributions of x_{eff} in the data for each class in Figure 4.

4.4 Study of the mistag rate and the discriminating variables

The compatibility between the mistag rate in the data and the Monte Carlo can be checked by measuring the mistag fraction for all classes combined with a likelihood composed of the total distribution of the discriminating variables in the data:

$$\mathcal{L}(\eta) = \prod^{classes} \prod_i \frac{1}{1+\zeta} \left((1-\eta) R(x_{eff}^i) + \eta W(x_{eff}^i) + \zeta B(x_{eff}^i) \right). \tag{15}$$

The inner product is over all events in a given class. The measured value, η_{meas}, is that which maximizes the likelihood function. The measured mistag rate for all classes combined is $\eta_{meas} = (37 \pm 12)\%$ which is in agreement with the value obtained from the Monte Carlo, $\eta_{MC} = (36 \pm 3)\%$. Despite the rather coarse precision of this measurement, the observed agreement demonstrates that the x_{eff} distributions are well described by the Monte Carlo simulation.

The effective power of the tagging method is not given by the value of η. Even for a value of η close to 50% the use of the discriminating variables ensures that the initial state of the B_s^0 can be tagged. In standard tagging techniques [4, 5, 6, 7], a dilution factor D is introduced ($D \equiv efficiency \times (1-2\eta)^2$) to account for the loss of information due to the tagging method. In the case of the present analysis, the above formula does not apply but an equivalent dilution factor [26] can be obtained, $D = 0.218 \pm 0.029$, which corresponds to an effective mistag value of $(27 \pm 2)\%$ with the 100% tagging efficiency of this analysis. Table 4 shows the effective mistag rate for each class.

Although the comparison of η_{meas} and η_{MC} is favourable within the small statistical sample available, the distributions of each discriminating variable in data and $Z \to q\bar{q}$ Monte Carlo are compared directly with an event sample that is enlarged with looser vertex requirements and wider mass windows. The reconstructed jet charge distributions for both the data and the Monte Carlo

samples are fitted with a sum of two Gaussians where the discrepancy between the data and the simulation is parametrized in terms of an overall offset of the mean jet charge and an overall scale factor in the widths. A similar procedure is applied to χ_π for the fragmentation kaon. The results for the offset δ and the scale factor $\mathcal{S}_v$ are given in Table 5. For the rescaled momentum Z_K the possibility of a linear transformation, $Z_K \to \delta + \mathcal{S}_v \times Z_K$, is allowed, and the result of the fit is also presented in Table 5. Such a transformation could be due to incorrect modeling of the fragmentation in the simulation, for example. As seen in Table 5, there is relatively good agreement between the data and the Monte Carlo.

For the opposite hemisphere lepton, the transverse momentum $p_T(\ell)$ with respect to the jet axis has been shown to be adequately simulated by the Monte Carlo [30].

Class	$D_s^- \ell^+ \nu X$ mistag fraction (%)	$D_s^- \ell^+ \nu X$ effective mistag fraction (%)	$D_s^{(*)-} D^{(*)} X$ mistag fraction (%)	S_t
1	39 ± 2	34 ± 2	37 ± 1	1.13
2	32 ± 2	24 ± 1	42 ± 1	1.04
3	34 ± 3	23 ± 2	33 ± 1	1.15
4	18 ± 3	13 ± 2	30 ± 2	1.06
5	60 ± 5	24 ± 2	43 ± 2	1.06
6	37 ± 6	35 ± 7	42 ± 6	1.06
7	33 ± 14	23 ± 10	18 ± 9	1.11

Table 4: The second column lists the mistag rate for each class measured for the $B_s^0 \to D_s^- \ell^+ \nu X$ signal Monte Carlo. The third column contains the effective mistag rate for the $B_s^0 \to D_s^- \ell^+ \nu X$ Monte Carlo as described in section 4.4. Column 4 lists the mistag rate measured for the $\bar{B} \to D_s^{(*)-} D^{(*)} X$ background Monte Carlo. Looser reconstruction criteria are employed for the $\bar{B} \to D_s^{(*)-} D^{(*)} X$ events to obtain reasonable numbers of events in each class. The looser selection does not affect the mistag rate or the distribution of discriminating variables with respect to the standard cuts. The mistag uncertainty scale factor S_t in column 5 is described in section 4.4.

Variable	δ	$\mathcal{S}_v$
Q_o	$+0.006 \pm 0.005$	0.97 ± 0.02
Q_s	-0.010 ± 0.009	1.04 ± 0.02
χ_π	-0.025 ± 0.024	1.01 ± 0.02
Z_K	$+0.001 \pm 0.001$	0.95 ± 0.02

Table 5: The offset δ and scale factor $\mathcal{S}_v$ representing the difference between the Monte Carlo and the data for each discriminating variable, except $p_T(\ell)$, as described in the text.

An additional comparison is performed to quantify the overall agreement between the data and Monte Carlo for each class. A χ^2 is constructed from binned distributions of the discriminating

variables used in each class,

$$\chi^2 \equiv \sum_j^{N_v} \sum_i^{N_b} \frac{(N_{ij}^{MC} - N_{ij}^D)^2}{\omega_{ij}^2}, \tag{16}$$

where N_v is the number of discriminating variables in a given class and N_b is the number of bins for a given discriminating variable, N_{ij}^{MC} is the expected number of events determined from the Monte Carlo, N_{ij}^D is the observed number of events in the ith bin for the jth class and ω_{ij} is the statistical uncertainty on $N_{ij}^{MC} - N_{ij}^D$. The mistag uncertainty scale factors are then $S_t \equiv \sqrt{\chi^2/(N_c N_b - 1)}$ using the procedure recommended in [16] and shown in Table 4.

The agreement between the data and the simulation is satisfactory and the small observed deviations, $\mathcal{S}_v$, δ and S_t, will be used to estimate systematic effects in the final results.

5 The likelihood function

A likelihood function can now be written with components similar to that of the B_s^0 lifetime measurement [15] with the addition of the tagging information described in section 4.3:

$$\begin{aligned}
\mathcal{L}(\tau_s, \Delta m_s) &= \prod_i^{N_m} \left[(1 - X_{eff}^i) \tilde{\mathcal{P}}_m(t_m^i; \tau_s, \Delta m_s) + X_{eff}^i \tilde{\mathcal{P}}_u(t_m^i; \tau_s, \Delta m_s) + Z_{eff}^i \tilde{\mathcal{P}}_{bk}(t_m^i) \right] \\
&\times \prod_i^{N_u} \left[(1 - X_{eff}^i) \tilde{\mathcal{P}}_u(t_m^i; \tau_s, \Delta m_s) + X_{eff}^i \tilde{\mathcal{P}}_m(t_m^i; \tau_s, \Delta m_s) + Z_{eff}^i \tilde{\mathcal{P}}_{bk}(t_m^i) \right], \quad (17)
\end{aligned}$$

where the products run over the number of events tagged as "mixed" (N_m) and "unmixed" (N_u).

The functions $\tilde{\mathcal{P}}_m(t_m^i; \tau, \Delta m)$ and $\tilde{\mathcal{P}}_u(t_m^i; \tau, \Delta m)$ represent the proper time distribution of events which are mixed and unmixed, Equations 1 and 2, respectively, after convolution with the event-dependent proper time resolution of the detector (section 3). The mistag probability for the ith event is $X_{eff}^i \equiv X_{eff}(x_{eff}^i)$ from Equation 12 and the event-by-event relative background fraction is $Z_{eff}^i \equiv Z_{eff}(x_{eff}^i)$ from Equation 13.

The proper time distribution of the background, $\tilde{\mathcal{P}}_{bk}$, has three components:

$$\tilde{\mathcal{P}}_{bk}(t_m^i) = r_{comb} \tilde{\mathcal{P}}_{comb}(t_m^i) + r_{DsD} \tilde{\mathcal{P}}_{DsD}(t_m^i) + r_{refl} \tilde{\mathcal{P}}_{refl}(t_m^i), \tag{18}$$

where $r_{comb} + r_{DsD} + r_{refl} = 1$ are the fractions of combinatorial, $\bar{B} \to D_s^{(*)-} D^{(*)} X$ and reflection background calculated for each decay mode (Table 1).

- $\tilde{\mathcal{P}}_{comb}(t_m^i)$ is the proper time distribution of the combinatorial background and is estimated from the "sidebands" as in the lifetime measurement [15].

- For the $\bar{B} \to D_s^{(*)-} D^{(*)} X$ background, the tagging of the final state is reversed with respect to semileptonic B_s^0 decays because the D_s^- comes from the virtual W^-. The fraction of $\bar{B} \to D_s^{(*)-} D^{(*)} X$ background that can oscillate with the frequency Δm_d is f_d, the fraction of B_d^0 produced in $Z \to b\bar{b}$ decays. The proper time dependence of the $\bar{B} \to D_s^{(*)-} D^{(*)} X$ background is

$$\tilde{\mathcal{P}}_{DsD}(t_m^i) = f_d \left[(1 - \eta_d) \tilde{\mathcal{P}}_u(t_m^i; \tau_d, \Delta m_d) + \eta_d \tilde{\mathcal{P}}_m(t_m^i; \tau_d, \Delta m_d) \right] + (1 - f_d) \tilde{\mathcal{P}}(t_m^i; \hat{\tau}_b), \tag{19}$$

where η_d is the class-dependent mistag rate for the $\bar{B} \to D_s^{(*)-} D^{(*)} X$ process (Table 4), $\tilde{\mathcal{P}}(t_m^i; \tau)$ is the expected proper time distribution for a lifetime τ, τ_d is the B_d^0 lifetime, and $\hat{\tau}_b$ is the

abundance–weighted average of the B_s^0, B^+ and b baryon lifetimes. The component of this background from the B_s^0 is due to the process $\bar{B}_s^0 \rightarrow D_s^{(*)-} D_s^{(*)+} X$ followed by the semileptonic decay of either the $D_s^{(*)-}$ or the $D_s^{(*)+}$. Thus the oscillatory behaviour of this small fraction of the $\bar{B} \rightarrow D_s^{(*)-} D^{(*)} X$ background cancels on average.

- The reflection background ($D^- \rightarrow K^{*0}\pi^-$ misidentified as $K^{*0}K^-$) is dominated by $B_d^0 \rightarrow D^{(*)-}\ell^+\nu X$ so

$$\tilde{\mathcal{P}}_{refl}(t_{\rm m}^i) = (1 - \eta_r)\tilde{\mathcal{P}}_m(t_{\rm m}^i; \tau_d, \Delta m_d) + \eta_r \tilde{\mathcal{P}}_u(t_{\rm m}^i; \tau_d, \Delta m_d), \tag{20}$$

where η_r is the class-dependent mistag rate for semileptonic B_d^0 decays.

6 Study of $B_s^0 \bar{B}_s^0$ oscillations

The B_s^0 lifetime τ_s in the likelihood function (Equation 17) is fixed at the value $\langle \tau_s \rangle$ which maximizes the likelihood in the absence of mixing and then $\mathcal{L}(\Delta m_s) \equiv \mathcal{L}(\langle \tau_s \rangle, \Delta m_s)$ is evaluated. Monte Carlo studies show that this procedure slightly improves the accuracy of a low Δm_s measurement. The value of the B_s^0 lifetime which maximizes the likelihood is $1.55 ^{+0.14}_{-0.13} (stat) \pm 0.01 (syst)$ ps where only the systematic uncertainty due to the X_{eff} and Z_{eff} distributions is quoted and accounts for the slight difference with the result shown in section 3.

The log of the likelihood as a function of Δm_s, $\Delta L(\Delta m_s) \equiv \log \mathcal{L}_{max} - \log \mathcal{L}(\Delta m_s)$, is presented in Figure 5(a), where $\mathcal{L}_{\max}$ is the maximum value of the likelihood. The result indicates that low values of Δm_s are strongly disfavoured but that no single value of Δm_s is significantly preferred. The approximately constant value of $\Delta L(\Delta m_s)$ for large Δm_s reflects the inability of the data to distinguish between different large values of Δm_s, as expected due to the limited proper time resolution and number of events.

6.1 Description of the fast Monte Carlo simulation

In order to determine which values of Δm_s are excluded at a given confidence level, the behaviour of $\Delta L(\Delta m_s)$ is studied with a fast Monte Carlo simulating the detector response, the rate of the signal and background processes, their reconstructed decay length and momentum distributions, the distributions of the discriminating variables and the mistag rates. For each simulated experiment in the fast Monte Carlo, each parameter listed in Table 6 is chosen randomly from a Gaussian distribution around its central value with a width equal to its uncertainty. The mistag rate for the signal for each class is chosen in a similar way, except that the width of the Gaussian is multiplied by the scale factor $S_{\rm t}$ listed in Table 4. For the generation of the relative fraction of B_s^0 signal and $\bar{B} \rightarrow D_s^{(*)-} D^{(*)} X$ background, the uncertainty in the background production rate (Table 2) is conservatively assumed to be 100% correlated with the uncertainty in $f_{\rm s}$, the B_s^0 production rate (Table 6).

Two additional effects are included for which the method of random Gaussian variation described above cannot be applied: the proper time distribution of the combinatorial background $\tilde{\mathcal{P}}_{comb}(t_{\rm m})$ and the distributions of the discriminating variables. The sensitivity to $\tilde{\mathcal{P}}_{comb}(t_{\rm m})$ is determined by analyzing each simulated experiment with either $\tilde{\mathcal{P}}_{comb}(t_{\rm m})$ determined from the like-sign sidebands $\tilde{\mathcal{P}}^+_{comb}(t_{\rm m})$ or the unlike-sign sidebands $\tilde{\mathcal{P}}^-_{comb}(t_{\rm m})$ as in the B_s^0 lifetime measurement [15].

The sensitivity of the analysis to the details of the distributions of the discriminating variables is determined by producing modified distributions $r_i^\pm$ and $w_i^\pm$. For $Q_{\rm o}$, $Q_{\rm s}$ and χ_π these are obtained by offsetting the distributions r_i and w_i by $\pm|\delta|$ and multiplying their widths by $1 \pm |1 - \mathcal{S}_{\rm v}|$, where δ and $\mathcal{S}_{\rm v}$ are given in Table 5. For $Z_{\rm K}$ the linear transformation, $Z_{\rm K} \rightarrow \pm|\delta| + (1 \pm |1 - \mathcal{S}_{\rm v}|) \times Z_{\rm K}$, is

used. With these definitions, the power of a given discriminating variable x_i is reduced (or enhanced) when the distributions r_i^+ and w_i^+ (or r_i^- and w_i^-) are used instead of r_i and w_i. In order to estimate the systematic effect of the shape of the low $p_T(\ell)$ region, which is sensitive to the estimation of the contribution of cascade decay (b $\rightarrow$ c $\rightarrow \ell$), the distributions in the $p_T(\ell) < 1$ GeV/c region are replaced by flat distributions to create both $r^\pm(p_T(\ell))$ and $w^\pm(p_T(\ell))$. This is equivalent to the assumption that only the fractions of events in this region are reliable, but not the details of the distributions. The distributions r_i^+ and w_i^+ (or r_i^- and w_i^-) are then used to calculate x_{eff}^+ (x_{eff}^-) according to Equation 11, and the procedure described in section 4.3 is followed to produce two sets of modified x_{eff} distributions, $R^\pm(x_{eff}^\pm)$, $W^\pm(x_{eff}^\pm)$ and $B^\pm(x_{eff}^\pm)$.

Finally, to incorporate these "non-Gaussian" effects into the fast Monte Carlo, 600 experiments are generated with one set of the modified x_{eff} distributions, R^+, W^+ and B^+, and 600 experiments are generated with R^-, W^- and B^- at a given value of Δm_s. Half of each set of 600 experiments is analyzed with $\tilde{\mathcal{P}}_{comb}^+$ and half with $\tilde{\mathcal{P}}_{comb}^-$ resulting in a total of 1200 fast simulated experiments at each value of Δm_s.

The generation of a single event proceeds as follows:

1. The decay mode is selected based on the observed number of events per mode (Table 1).

2. The decay source, either the signal or one of the possible backgrounds, is selected based on the observed signal and background rates for the selected decay mode.

3. For signal, $\bar{\mathrm{B}}_{\mathrm{d}}^0 \rightarrow \mathrm{D}_{\mathrm{s}}^{(*)-}\mathrm{D}^{(*)}X$ or reflection background events, the true mixed or unmixed final state of the event is randomly chosen based on the expected fraction of mixed events,

$$\chi \equiv \frac{1}{2} \times \frac{(\tau \Delta m)^2}{1 + (\tau \Delta m)^2}. \tag{21}$$

4. For the signal and non-combinatorial background events, a true momentum is generated based on appropriate momentum spectrum obtained from the full Monte Carlo simulation. A true proper time is also chosen from an exponential decay time distribution modulated by an oscillatory term for $\mathrm{B}_{\mathrm{s}}^0 \rightarrow \mathrm{D}_{\mathrm{s}}^- \ell^+ \nu X$, $\bar{\mathrm{B}}_{\mathrm{d}}^0 \rightarrow \mathrm{D}_{\mathrm{s}}^{(*)-}\mathrm{D}^{(*)}X$ or reflection background events. The true decay length is then calculated from the true momentum and proper time. The measured decay length uncertainty is generated from the σ_{L} distribution from full Monte Carlo events. A reconstructed decay length is obtained by smearing the true decay length by $S_{\mathrm{L}} \times \sigma_{\mathrm{L}}$ with $S_{\mathrm{L}} = S_{\mathrm{L}}(h)$ or $S_{\mathrm{L}} = S_{\mathrm{L}}(\ell)$ for hadronic or semileptonic $\mathrm{D}_{\mathrm{s}}^-$ decay modes, respectively. The momentum resolution varies somewhat as a function of the true momentum. The reconstructed momentum is smeared accordingly, using one of four slices in momentum.

5. For combinatorial background, the distributions of the measured momentum, decay length and decay length uncertainty are taken from the calculated distributions obtained from the "sidebands".

6. The tagging class of the event is now generated based on the observed number of events per class (Table 3), and each event is either assigned as a right or wrong tag based on the mistag rate for each class for the signal and non-combinatorial background (Table 4). For the combinatorial background, the mixed or unmixed state is determined from the fraction of data "sidebands" events tagged as mixed or unmixed.

7. Finally, a value of x_{eff} is generated for each signal or non-combinatorial background event from the $R^\pm(x_{eff})$ or $W^\pm(x_{eff})$ distributions based on the tagging class and whether the event is

12

a right or wrong tag. For background events, the x_{eff} value is generated from the $B^{\pm}(x_{eff})$ distributions based on the tagging class and the decay mode.

Each fast Monte Carlo experiment is generated with 277 events at a given value of Δm_s and analyzed as the data. At each input value of Δm_s, $\Delta L^{95}(\Delta m_s)$ is defined such that 95% of the fast Monte Carlo experiments have $\Delta L(\Delta m_s) < \Delta L^{95}(\Delta m_s)$. A new set of 1200 experiments is generated for different input values of Δm_s (1, 2, 3, 4, 5, 6, 7, 8, 12, and 16 ps^{-1}) to produce the points corresponding to the $\Delta L^{95}(\Delta m_s)$ curve shown in Figure 5(a). Additional sets of fast Monte Carlo experiments are generated at $\Delta m_s = 1$, 3, 6 and 12 ps^{-1} without the systematic variations described above in order to ascertain the overall impact on the 95% CL curve of the systematic uncertainties. The resulting 95% CL curve is shown in Figure 5(a) and differs from the 95% CL curve with the full systematics by about 0.3 in $\Delta L(\Delta m_s)$ at small Δm_s, mainly due to the uncertainty in the mistag rates and the sample purity.

Parameter	Value and uncertainty			Reference
τ_s	1.551	$\pm$	0.106 ps	[31]
τ_d	1.564	$\pm$	0.048 ps	[31]
τ_-	1.617	$\pm$	0.046 ps	[31]
τ_{baryon}	1.179	$\pm$	0.072 ps	[31]
Δm_d	0.465	$\pm$	0.022 ps^{-1}	[1]
a	3.1	$\pm$	0.2 GeV/c	Section 3
b	0.873	$\pm$	0.006	Section 3
σ_p	3.1	$\pm$	0.4 GeV/c	Section 3
$S_{\rm L}(\ell)$	1.42	$\pm$	0.11	Section 3
$S_{\rm L}(h)$	1.19	$\pm$	0.11	Section 3
$f_{\rm d}$	0.385	$\pm$	0.021	[15, 32, 33]
$f_{\rm s}$	0.102	$\pm$	0.016	[15, 32, 33]
f_{baryon}	0.128	$\pm$	0.039	[15, 32, 33]

Table 6: Parameters and their uncertainties used as input for the fast Monte Carlo. The abundance-weighted average $\hat{\tau}_b$, discussed following Equation 19, is derived from the b hadron lifetimes and fractions listed in the table. τ_- and τ_{baryon} are the B$^-$ and the b baryon lifetimes, respectively.

6.2 Results

The $\Delta L^{95}(\Delta m_s)$ curve constructed from the fast simulation intersects the log likelihood curve for the data at $\Delta m_s = 6.6$ ps^{-1}. Therefore, values of Δm_s less than 6.6 ps^{-1} are excluded at 95% confidence level.

A 95% CL lower limit greater than that observed in the data ($\Delta m_s > 6.6$ ps^{-1}) is found in 22% of 500 fast Monte Carlo experiments generated with near-maximal mixing ($\Delta m_s = 30$ ps^{-1}). Half of these experiments yield a lower limit above 4.3 ps^{-1}. The average $\Delta L(\Delta m_s)$ of these 500 experiments, $\langle \Delta L \rangle$, is displayed in Figure 5(a) and intersects the $\Delta L^{95}(\Delta m_s)$ curve at $\Delta m_s = 7.5$ ps^{-1}. The median limit of 4.3 ps^{-1} is significantly lower than this crossing point, because of large statistical fluctuations of the individual $\Delta L(\Delta m_s)$ curves.

The confidence level $c(\Delta m_s)$ for a given Δm_s hypothesis is obtained in a similar way and is shown in Figure 5(b). The same procedure is also applied to $\langle \Delta L \rangle$ with a generated value of $\Delta m_s = 30$ ps^{-1} to determine the confidence level expected on average when Δm_s is large ($\equiv \langle c(\Delta m_s) \rangle$).

6.3   Comparison with previous results

The fraction f_s of B$_s^0$ mesons produced in Z $\to b\bar{b}$ decays influences both the fraction of candidates attributed to the B$_s^0$ meson and the purity of an opposite hemiphere tag. In previous B$_s^0\bar{B}_s^0$ mixing studies by ALEPH [4, 5, 6] DELPHI [7] and OPAL [8], the calculated B$_s^0$ meson fraction is directly proportional to f_s whilst in this analysis, f_s enters only at second order via the calculation of the $\bar{B} \to D_s^{(*)-}D^{(*)}X$ fraction. The purity of an opposite hemisphere tag and the associated discriminating variables depends on f_s via the average fraction of Z $\to b\bar{b}$ events which experience mixing, $\bar{\chi} = f_s\chi_s + f_d\chi_d$. Both the effect on the calculated B$_s^0$ meson fraction and the tagging purity due to variations in f_s are included in the overall systematic uncertainty embodied in the $\Delta L^{95}(\Delta m_s)$ and $c(\Delta m_s)$ curves shown in Figure 5.

The 95% CL of $\Delta m_s > 6.6$ ps^{-1} presented here is not fully statistically independent from the three previous ALEPH results obtained from inclusive leptons in approximately 3.3×10^6 hadronic Z decays with either an opposite hemisphere lepton tag ($\Delta m_s > 5.6$ ps^{-1} for $f_s = (12.2 \pm 3.1)\%$ [4][4]), a jet charge tag ($\Delta m_s > 6.1$ ps^{-1} for $f_s = 12\%$ [5]), or a combined fragmentation kaon and jet charge tag ($\Delta m_s > 3.9$ ps^{-1} for $f_s = (12.2 \pm 3.5)\%$ [6][4]). The OPAL collaboration obtained a lower limit of $\Delta m_s > 3.3$ ps^{-1} assuming $f_s = (12.0 \pm 3.6)\%$ [8][4] with a jet charge tag in approximately 3×10^6 hadronic Z decays whilst DELPHI employed a method combining lepton and jet charge tags to set a limit at $\Delta m_s > 4.2$ ps^{-1} in about 3.2×10^6 hadronic Z decays assuming $f_s = (10 \pm 3)\%$ [7][4] (All lower limits are at 95% confidence level.)

7   Conclusion

A new method of initial state tagging has been applied to a sample of 277 D$_s^-\ell^+$ combinations indicative of B$_s^0$ semileptonic decay obtained from approximately four million hadronic Z decays. This method fully exploits the statistically limited sample of events, taking into account the precise time reconstruction and the detailed tagging information available for the whole event. Contrary to the results based on inclusive semileptonic decay modes used in previous analyses, this result depends very weakly on the fraction of b quarks which produce B$_s^0$ mesons, f_s. The behaviour of the likelihood as a function of Δm_s has been evaluated in order to set limits on the values of Δm_s allowed by the experimental data. B$_s^0\bar{B}_s^0$ oscillation frequencies less than 6.6 ps^{-1} are excluded at 95% confidence level.

The B$_s^0$ lifetime measurement using D$_s^-\ell^+$ combinations has been updated. The result, $\tau_s = 1.54 ^{+0.14}_{-0.13} (stat) \pm 0.04 (syst)$ ps, supersedes the previous ALEPH measurement [15].

---

[4]Preliminary conference results.

References

[1] R. Aleksan, plenary talk, to be published in the proceedings of the International Europhysics Conference on High Energy Physics, Brussels, Belgium, 1995.

[2] A.J. Buras, M. Jamin and P.H. Weisz, Nucl. Phys. **B347** (1990) 491.

[3] A. Ali and D. London, Z. Phys. **C65** (1995) 431.

[4] D. Buskulic *et al.*, ALEPH Collaboration, Phys. Lett. **B322** (1994) 441;
ALEPH Collaboration, "Measurement of the $B_d^0 \bar{B}_d^0$ oscillation frequency", submitted to the International Europhysics Conference on High Energy Physics, Brussels, Belgium, 1995, reference eps0409.

[5] D. Buskulic *et al.*, ALEPH Collaboration, Phys. Lett. **B356** (1995) 409.

[6] ALEPH Collaboration, "Time dependent B_s^0 mixing from lepton-kaon correlations", submitted to the International Europhysics Conference on High Energy Physics, Brussels, Belgium, 1995, reference eps0410.

[7] DELPHI Collaboration, "Improved measurement of the oscillation frequencies of B^0 mesons", submitted to the International Europhysics Conference on High Energy Physics, Brussels, Belgium, 1995, reference eps0568.

[8] R. Akers *et al.*, OPAL Collaboration, Z. Phys. **C66** (1995) 555;
OPAL Collaboration, "A study of B meson oscillation using inclusive lepton events", submitted to the International Symposium on Lepton-Photon Interactions, Beijing, China, (1995).

[9] D. Decamp *et al.*, ALEPH Collaboration, Nucl. Instrum. Methods **A294** (1990) 121;
G. Batignani *et al.*, 1991 IEEE Nuclear Science Symposium, Santa Fe, IEEE Trans. Nucl. Sci. NS-39(4/5) (1992) Vol. 1, p. 438.

[10] D. Buskulic *et al.*, ALEPH Collaboration, Nucl. Instrum. Methods **A360** (1995) 481.

[11] D. Decamp *et al.*, ALEPH Collaboration, Z. Phys. **C53** (1992) 1.

[12] D. Buskulic *et al.*, ALEPH Collaboration, Phys. Lett. **B313** (1993) 535.

[13] T. Sjöstrand and M. Bengtsson, Computer Phys. Commun. **43** (1987) 367.

[14] J. Körner and G. Schuler, Z. Phys. **C38** (1988) 511.

[15] D. Buskulic *et al.*, ALEPH Collaboration, Phys. Lett. **B361** (1995) 221.

[16] L. Montanet *et al.*, Particle Data Group, Phys. Rev. **D50** (1994) 1173.

[17] J. Gronberg *et al.*, CLEO Collaboration, "Observation of the Isospin-Violating Decay $D_s^{*-} \to D_s^- \pi^0$", submitted to the International Europhysics Conference on High Energy Physics, Brussels, Belgium, 1995, reference eps0177, CLEO CONF 95-17.

[18] D. Buskulic *et al.*, ALEPH Collaboration, Phys. Lett. **B322** (1994) 275.

[19] T. Bergfeld *et al.*, CLEO Collaboration, "Measurements of $B \to D_s^+ X$ Decays", contribution to the 27th International Conference on High Energy Physics, Glasgow, Scotland, 20-27 July, 1994, ICHEP94 reference 0246 and CLEO preprint CLEO CONF 94-9.

[20] H. Albrecht *et al.*, ARGUS Collaboration, Z. Phys. **C54** (1992) 1.

[21] ALEPH, DELPHI, L3, OPAL and The LEP Electroweak Working Group, "Combined Preliminary Data on Z Parameters from the LEP Experiments and Constraints on the Standard Model," CERN-PPE/94-187.

[22] D. Buskulic *et al.*, ALEPH Collaboration, Phys. Lett. **B313** (1993) 498.

[23] P. Abreu *et al.*, DELPHI Collaboration, Phys. Lett. **B338** (1994) 409.

[24] R. Akers *et al.*, OPAL Collaboration, Phys. Lett. **B327** (1994) 411.

[25] ALEPH Collaboration, "The Measurement of the Time Dependence of $B_d^0\bar{B}_d^0$ Mixing using D^*-Lepton and D^*-Jet Charge Correlations", (1994) ICHEP94 reference 0576.

[26] D. E. Jaffe, F. Le Diberder and M.-H. Schune, LAL 94–67 and FSU-SCRI 94–101.

[27] D. Buskulic *et al.*, ALEPH Collaboration, Nucl. Instrum. Methods **A346** (1994) 461.

[28] A. Ali and F. Barreiro, Z. Phys. **C30** (1986) 635.

[29] M.R. Adams *et al.*, Phys. Rev. **D50** (1994) 1836.

[30] D. Buskulic *et al.*, ALEPH Collaboration, Z. Phys. **C62** (1994) 179.

[31] H.-G. Moser, "LEP B-Lifetimes", to be published in the proceedings of the International Europhysics Conference on High Energy Physics, Brussels, Belgium, 1995.

[32] O. Schneider, "$B_s^0\bar{B}_s^0$ Mixing", to be published in the proceedings of the International Europhysics Conference on High Energy Physics, Brussels, Belgium, 1995.

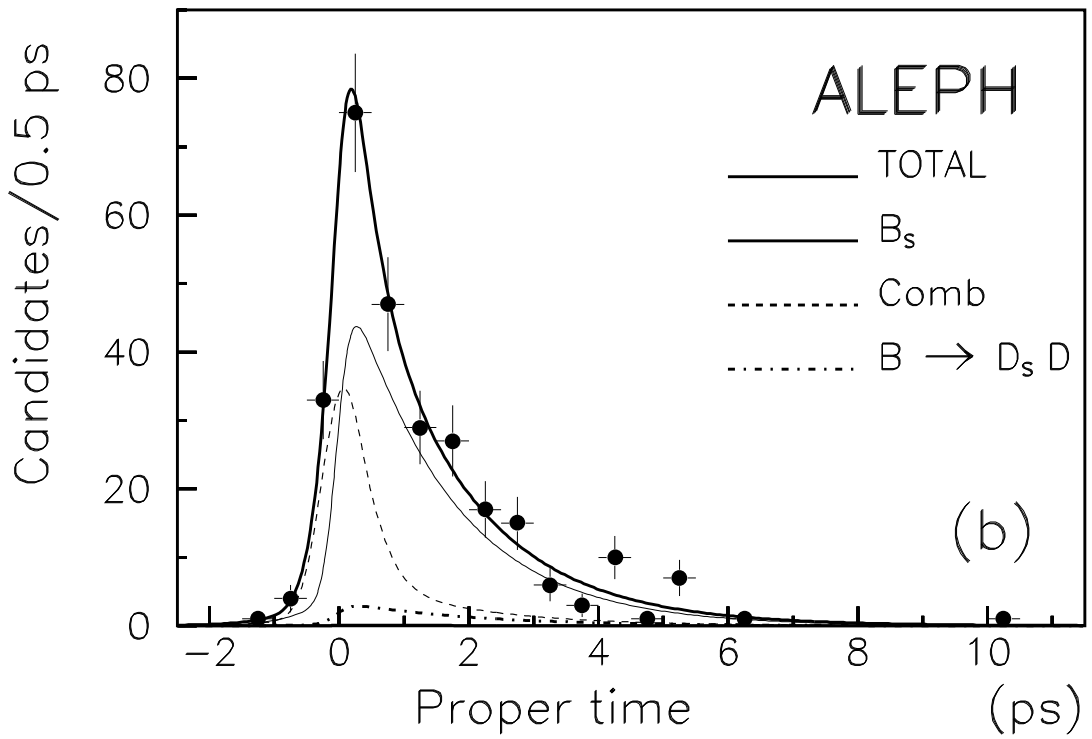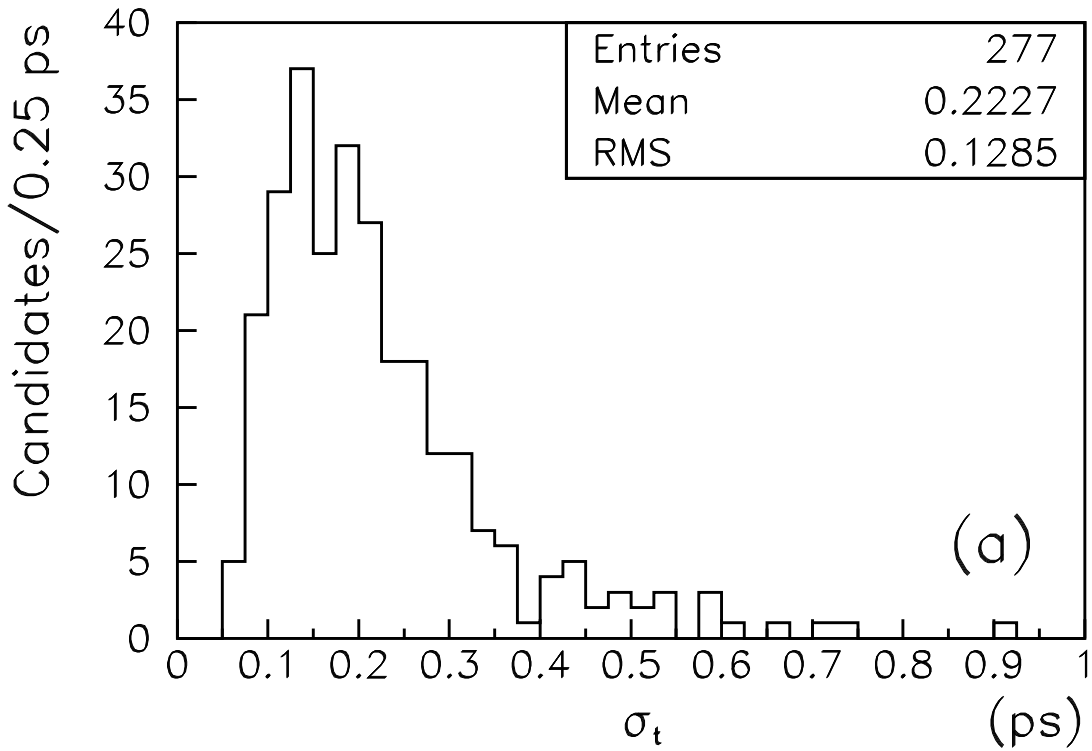[33] D. Buskulic *et al.*, ALEPH Collaboration, Phys. Lett. **B359** (1995) 236.

Figure 1: a) The calculated proper time resolutions for the 277 $D_s^- \ell^+$ candidates. b) The proper time distribution of the $D_s^- \ell^+$ candidates showing the fitted contributions of the B_s^0 signal, the combinatorial background and $\bar{B} \to D_s^{(*)-} D^{(*)} X$ background.
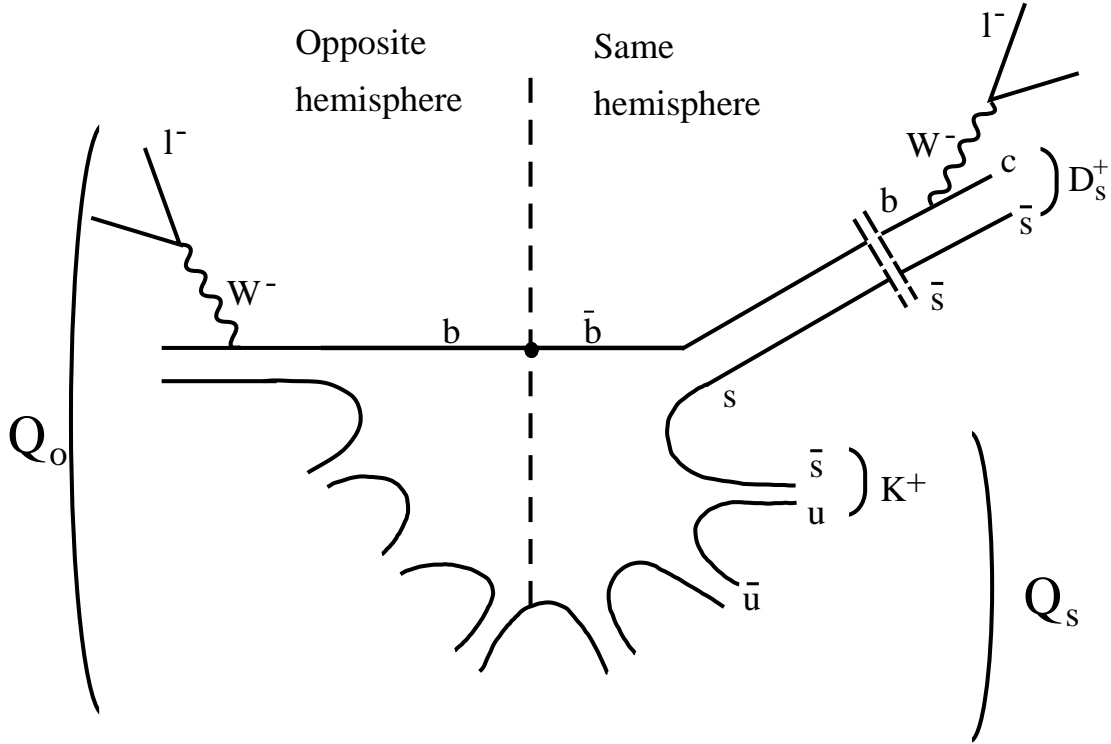
Figure 2: Schematic overview of a $Z \to b\bar{b}$ event where the $\bar{b}$ forms a B_s^0 which decays semileptonically as a $\bar{B}_s^0 \to D_s^+ \ell^- \bar{\nu}$. A fragmentation kaon, K^+, is produced in the same hemisphere as the $D_s^+ \ell^-$ combination, and the charged tracks from the fragmentation process can be combined to compute the same hemisphere jet charge Q_s. The b in the opposite hemisphere forms a b hadron which decays semileptonically yielding a tagging lepton, ℓ^-. In addition the opposite hemisphere jet charge Q_o can be computed from the combination of all charged tracks in the hemisphere.
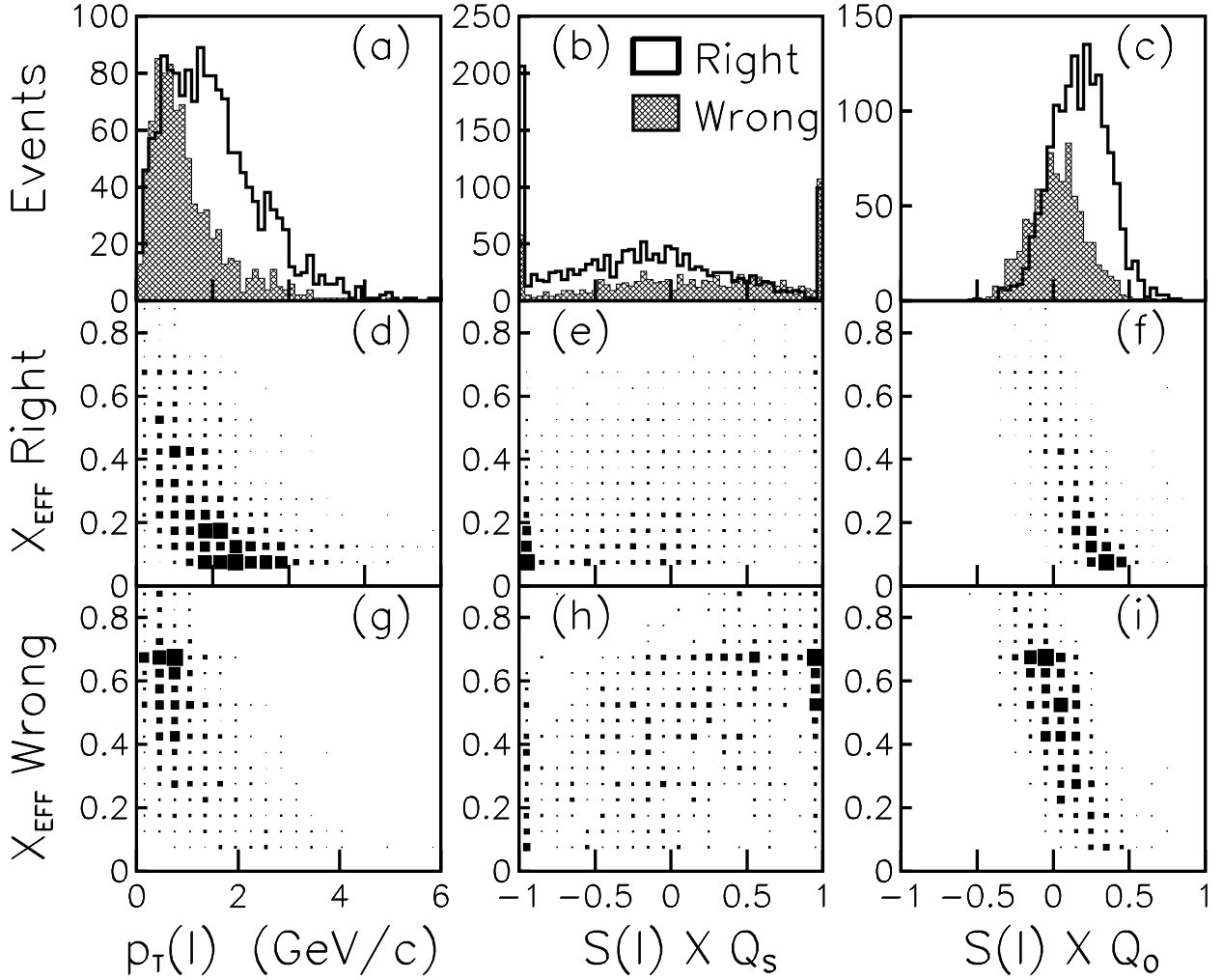
18

Figure 3: The $p_T(\ell)$, $S(\ell) \times Q_s$ and $S(\ell) \times Q_o$ spectra for right– and wrong–tag (shaded) events in class 3 are shown in (a), (b) and (c), respectively.

a) High $p_T(\ell)$ leptons generally identify the correct initial B_s^0 or $\bar{B}_s^0$ state while wrongly tagged events have lower momenta indicative of the cascade decay, b $\to$ c $\to \ell$. b) The lepton charge and Q_s generally have the opposite (same) sign when the lepton sign identifies the right (wrong) initial B_s^0 or $\bar{B}_s^0$ state as shown schematically in Figure 2. c) Some discriminating power is available in $S(\ell) \times Q_o$ as the lepton and Q_o have the same sign for correctly tagged events. The dependence of the mistag probability X_{eff} on the three discriminating variables is shown in (d–f) and (g-i) for right– and wrong–tag events, respectively. d) As expected, low mistag probabilities are associated with $p_T(\ell) > 1 GeV/c$ whilst correctly tagged events with lower $p_T(\ell)$ have increased mistag probabilities. Similarly, large, negative values of $S(\ell) \times Q_s$ (e) or positive values of $S(\ell) \times Q_o$ (f) correspond to events with low mistag probabilities. Frequently, events where the lepton charge predicts the wrong initial B_s^0 or $\bar{B}_s^0$ state are recognized as being mistagged by a low value of $p_T(\ell)$ (g), a large, positive value of $S(\ell) \times Q_s$ (h), a value of $S(\ell) \times Q_o \approx 0$ (i) or a combination of all three variables and are effectively transmuted into correctly tagged events by virtue of the $1 - X_{eff}$ term in Equation 17.
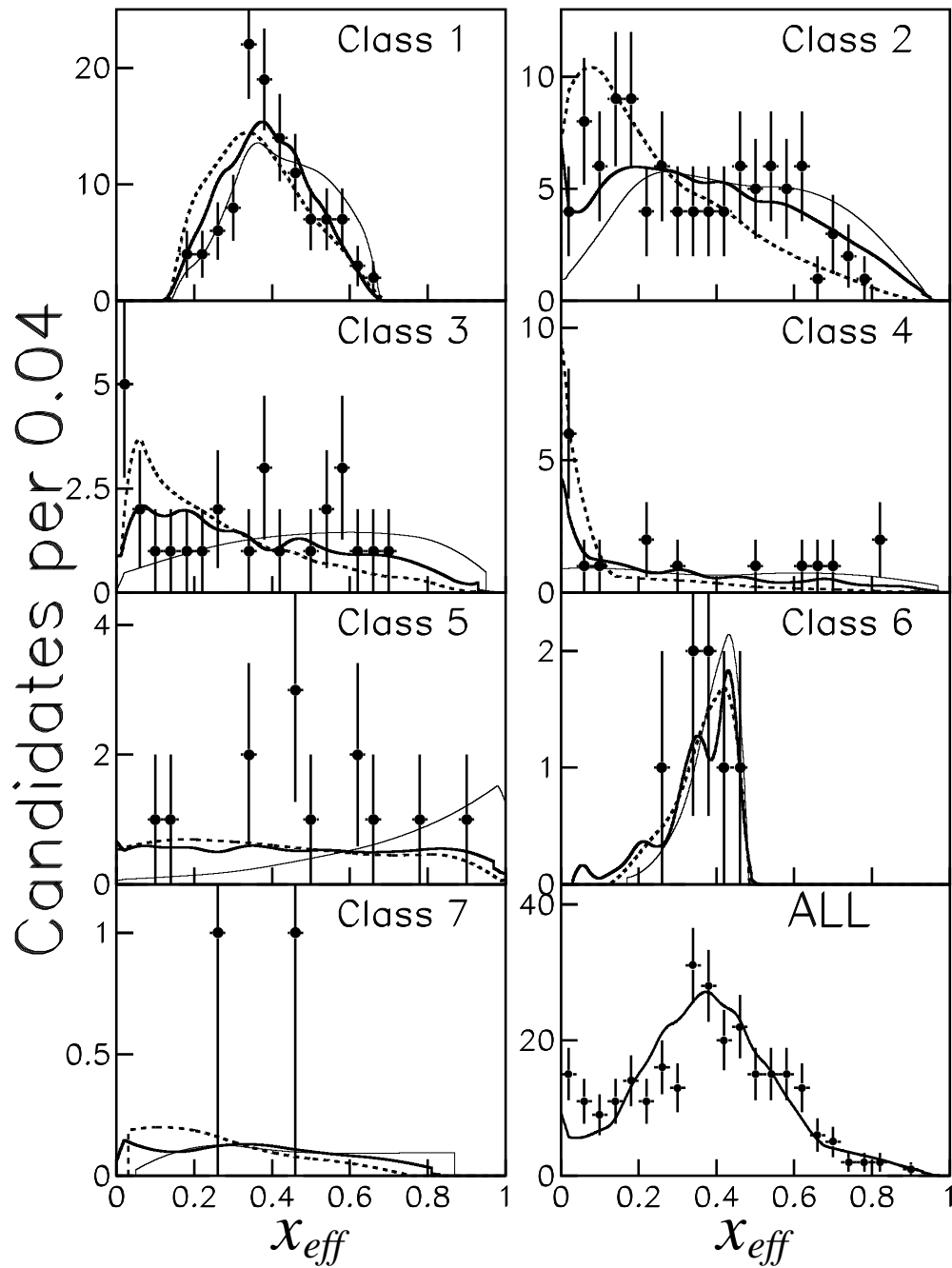
19

Figure 4: The distributions of x_{eff} observed in the data (points) for each class compared to the probability density distributions of x_{eff} for right–tags $R(x_{eff})$ (dashed curve) and wrong–tags $W(x_{eff})$ (thin curve) determined from Monte Carlo. The x_{eff} distributions due to background $B(x_{eff})$ (thick curve) are the weighted averages over the seven D_s^- decay modes. The undulations in the $B(x_{eff})$ curves result from the limited statistics available in the "sidebands". The plot in the lower right-hand corner shows the total distribution of x_{eff} observed in the data (points) compared with the weighted sum of the R, W and B distributions (solid curve). The curves are normalised to the number of events in each plot.
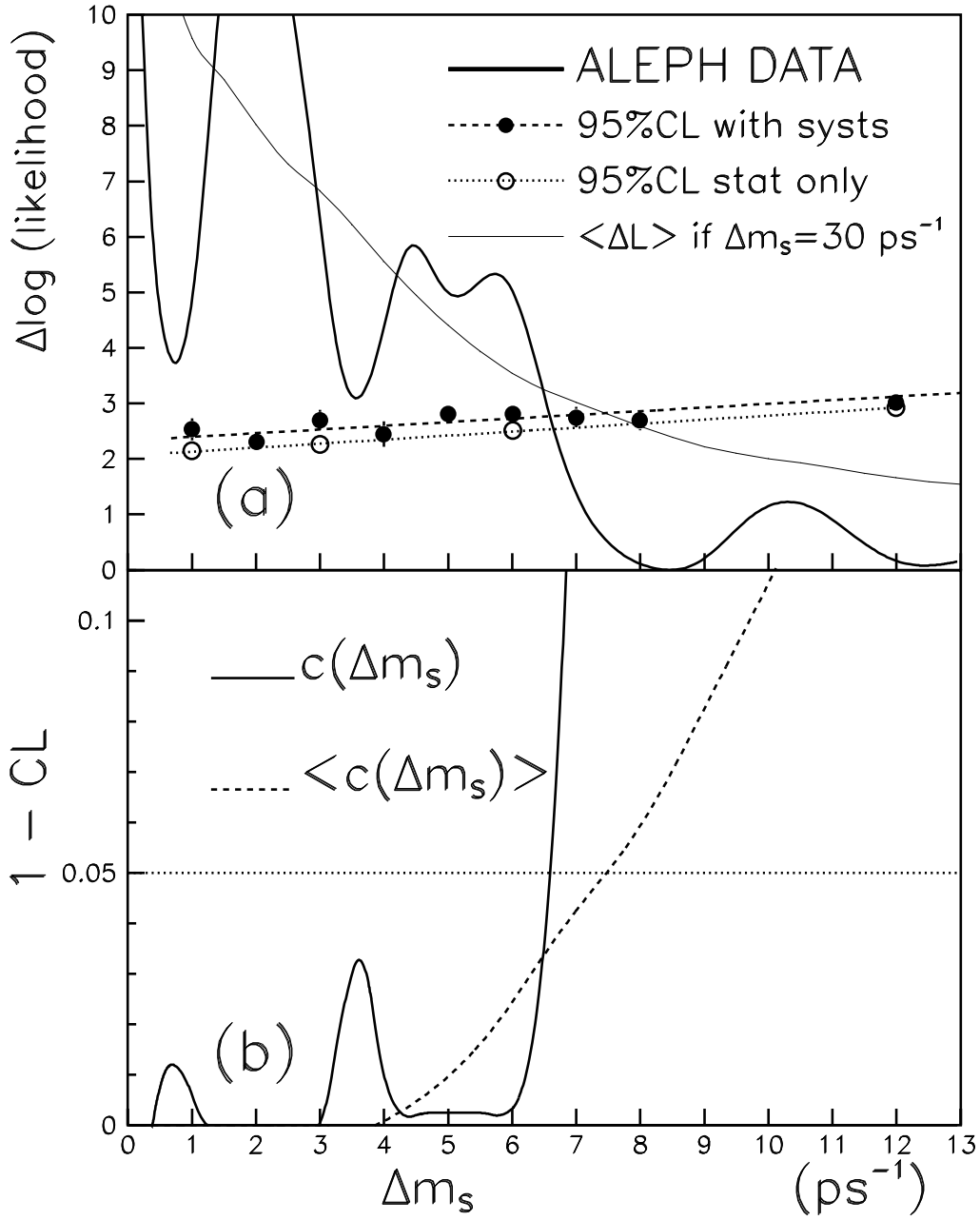
20

Figure 5: a) $\Delta L(\Delta m_s)$ for the data (solid curve), the 95% CL curve obtained from the fast Monte Carlo with (dashed) and without (dotted) the inclusion of systematic uncertainties. The thin solid curve shows the average behaviour of the likelihood if the true value of Δm_s is 30 ps^{-1}. b) The solid curve is $c(\Delta m_s) = 1 - CL$ calculated from the data and the $\Delta L(\Delta m_s)$ distributions from the fast simulation with the systematic effects included. The dashed curve is the average behaviour of the confidence level if the true value of Δm_s is 30 ps^{-1}.